Journal of Physics:
Conference Series

PAPER • OPEN ACCESS

Numerical simulation of hydrodynamic performance of AUV approaching an Underwater Charging Platform

To cite this article: Baowen Zhang *et al* 2026 *J. Phys.: Conf. Ser.* **3170** 012064

Numerical simulation of hydrodynamic performance of AUV approaching an Underwater Charging Platform

Baowen Zhang [1], Yazhou Zhu[2*], Yongquan Wang[2], Xiang Hu[1]

[1]College of ship and Ocean Engineering, Jiangsu University of Science and Technology, Zhenjiang 212000, China
[2]College of Ocean, Jiangsu University of Science and Technology, Zhenjiang 212000, China

[*]Corresponding author's e-mail: zhuyazhou@just.edu.cn

Abstract. The motion stability and safety of Autonomous Underwater Vehicle (AUV) are critical during their approach to underwater charging platforms. It is essential to analyze the hydrodynamic effects of the charging platform on AUV performance. This study employs Computational Fluid Dynamics (CFD) to solve the hydrodynamic parameters during the approach of an AUV to an underwater charging platform. Through numerical simulations, the flow field characteristics of the AUV near the platform are obtained, and the hydrodynamic responses under the coupled influence of factors such as AUV speed, distance from the platform, and angle of attack are analyzed. The results provide theoretical guidance for ensuring the stability and safety of the AUV's motion and attitude during docking with the underwater charging platform, offering valuable reference for the reliability design of related systems.

1. Introduction

China, as a maritime power with an extensive coastline, considers marine resources to be of vital importance. Autonomous Underwater Vehicle (AUV), as key operational platforms for marine development, play an increasingly crucial role in underwater detection and exploration[1]. AUV not only support offshore oil and gas resource development, modern aquaculture, and underwater environmental cleanup, but also contribute significantly to core capabilities such as underwater battlefield reconnaissance, navigation support, and emergency rescue operations[2-6]. Despite their wide applications, AUV face limitations in terms of operational duration and underwater data transmission capacity, necessitating periodic recovery for energy replenishment and data offloading.

An underwater charging platform can significantly extend the operational endurance and range of AUV by providing continuous energy supply and bidirectional data exchange[7]. During the docking process between the AUV and the platform, hydrodynamic interference between the two can occur. As the AUV approaches the underwater charging platform, the platform may affect the AUV's operational safety and stability. However, studies on the impact of underwater charging platforms on AUV are limited. Chen[8] investigated the flow field during submarine-AUV recovery, analyzing the hydrodynamic performance of the AUV in terms of pressure, vortex distribution, and velocity during the recovery process. Wu[9] studied the impact of the dock on AUV hydrodynamics, with results indicating minimal hindrance to AUV docking by the dock. Li[10] conducted numerical simulations on the vertical recovery dynamic process of a two-dimensional rotating body, analyzing the variations in fluid dynamics under different vertical speeds and pitch angles.

This study employs Computational Fluid Dynamics (CFD) numerical simulations to systematically investigate the hydrodynamic characteristics of AUV approaching an underwater charging platform under different operating conditions. By constructing a full three-dimensional viscous flow field model, the study analyzes the hydrodynamic responses under the coupled influence of multiple factors, including the AUV's spatial orientation (angle of attack), motion parameters (speed), and environmental constraints (distance from the platform). The findings provide theoretical guidance for ensuring the safe and stable motion and attitude control of AUV during docking with underwater charging platforms, and offer valuable insights for the reliability design of AUV-platform systems.

2. Numerical Methods

2.1. Computational Model

The computational model of the AUV and the underwater charging platform is shown in Figure 1. The AUV is an axisymmetric, flat-bodied vehicle with a main dimension of 7970 mm in length, 3530 mm in width, and 1900 mm in height. The underwater charging platform consists primarily of support legs, a charging plate, and connecting ribs. The support legs are 2500 mm in height, while the charging plate measures 8040 mm in length and 3360 mm in width.

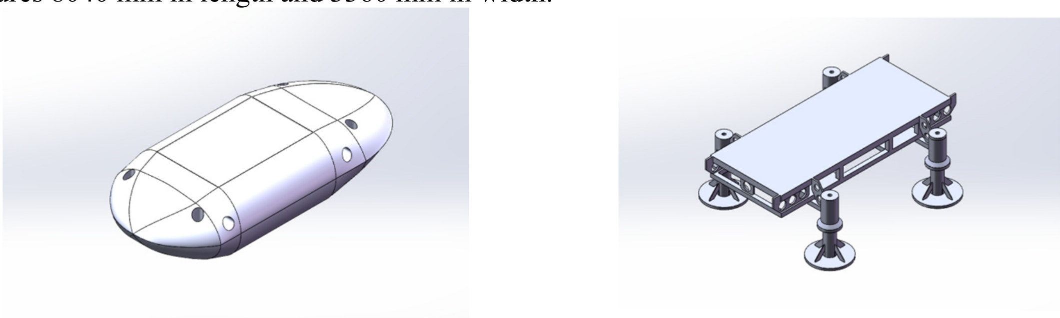

(a) (b)

Figure 1. (a) AUV Model. (b) Underwater Charging Platform Model.

2.2. Basic Governing Equations and Turbulence Models

For the hydrodynamic characteristics of the AUV, the working environment satisfies the conditions of viscous incompressibility. The flow field around the AUV can be described using the Navier-Stokes (N-S) equations, which are expressed as follows[10]:

$$\frac{\partial \overline{u}_i}{\partial x_i}=0 \tag{1}$$

$$\frac{\partial \overline{u}_i}{\partial t}+\frac{\partial \overline{u_i u_j}}{\partial x_j}=-\frac{1}{\rho}\frac{\partial p}{\partial x_i}+\frac{\partial}{x_j}\left(\mu\frac{\partial \overline{u}_i}{\partial x_j}-\overline{u'_i u'_j}\right)+g_i \tag{2}$$

The symbols used in the equations are defined as follows: $\overline{u}_i$ is the time-averaged velocity component; ρ is the fluid density; μ is the dynamic viscosity coefficient; g_i is the external volumetric force component in the x_i direction; t is time; p is the time-averaged pressure; $\overline{u'_i u'_j}$ is the Reynolds stress tensor.

This study adopts the Realizable k-epsilon turbulence model based on the RANS equations. Compared to the standard k-epsilon model, the Realizable model improves prediction accuracy for strong shear flows, flow separation, and vortex evolution by reconstructing the turbulence viscosity coefficient and the dissipation rate transport equation, while satisfying the realizability constraints of the Reynolds stress tensor. The two-layer approach used here avoids low Reynolds number treatment, making the model suitable for near-wall regions. During computation, the wall function solution and the external turbulence transport solution are coupled in the viscous sublayer, jointly solving for the global turbulent kinetic energy[11]. In the analysis of the AUV's hydrodynamic characteristics, including typical scenarios such as variations in angle of attack, flow separation at the tail, and attached-body interference, the Realizable k-epsilon model strikes a good balance between computational stability and accuracy.

2.3. Dimensionless Quantities and Coordinate Systems

This study aims to analyze the hydrodynamic characteristics of the AUV approaching the underwater charging platform. Given that the drag coefficient and lift coefficient are key hydrodynamic parameters for maneuvering control, the analysis and evaluation will focus on these two coefficients. The dimensionless quantities in this study include the drag coefficient, lift coefficient, and the spacing ratio H/h (where H is the vertical distance from the AUV's bottom to the upper surface of the underwater charging platform, and hhh is the height of the AUV).

The drag coefficient and lift coefficient are defined as follows[12]:

$$C_D = D / 0.5 \rho V^2 S_d \tag{3}$$

$$C_L = L / 0.5 \rho V^2 S_l \tag{4}$$

The symbols used in the equations are defined as follows: D is the drag, L is the lift, ρ is the fluid density, V is the inflow velocity, S_d is the projected area of the AUV in the direction of drag, and S_l is the projected area in the direction of lift.

In the present calculation, the coordinate system is set as shown in Figure 2. The flow velocity at the inlet is directed along the Z-axis, flowing from the positive to the negative direction. The drag is considered positive in the negative Z-direction, and the lift is defined as positive in the positive Y-direction.

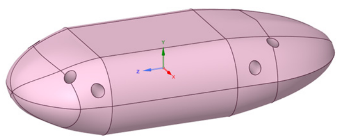

Figure 2. Coordinate System Diagram

3. Computational Domain and Mesh

3.1. Computational Domain and Mesh Division

The computational domain established in this study is a rectangular solution region. Taking the spacing ratio H/h=3 as an example, the simulation model and solution region for this condition are shown in Figure 3.

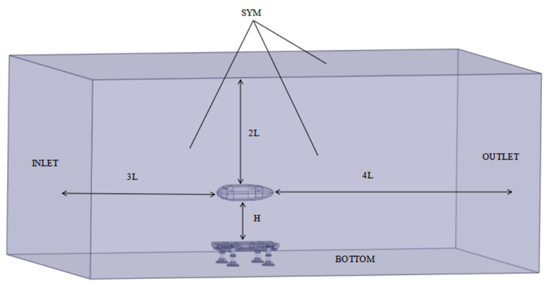

Figure 3. Computational Fluid Domain for a Spacing Ratio of 3.

The dimensions of the computational domain are 63,760 mm × 35,410 mm × 26,340 mm (length × width × height). The velocity inlet is located 4L away from the AUV's bow, and the pressure outlet is located 3L away from the AUV's stern. The AUV is positioned 2L from the top and symmetrical sides of the fluid domain. The distance from the AUV's bottom to the top of the underwater charging platform is 3h (the spacing ratio H/h=3). The underwater charging platform is located at the bottom of the fluid domain.

For the boundary conditions, the surface along the positive Z-direction of the computational domain is set as the velocity inlet boundary, and the surface along the negative Z-direction is set as the pressure outlet boundary. The AUV, underwater charging platform, and the bottom wall of the platform are set as no-slip walls, while other boundaries are treated as symmetry boundaries.

This study uses the Poly-Hexcore hybrid mesh to generate the volumetric mesh for the computational domain, with local refinement applied around the AUV, the charging platform, and the flow region at their aft. This method automatically generates structured hexahedral meshes in the core geometric areas, while using polyhedral elements near the wall surfaces and in regions with complex curvature to improve geometric fitting. A seamless connection is achieved through a common-node pyramid transition layer, minimizing non-conformal node errors.

3.2. *Mesh Independence Validation*

In CFD numerical calculations, the number of mesh cells is critical to computational accuracy. A coarse mesh has fewer cells and faster computation, but it often results in insufficient accuracy. A fine mesh, on the other hand, requires a large number of cells, which slows down the computation and significantly increases the demand for computational resources. Therefore, it is essential to determine an optimal mesh size that ensures computational accuracy while minimizing memory usage and improving computational efficiency.

In the following mesh independence study, three different meshes with varying numbers of cells were generated using the same meshing method for the case with a spacing ratio H/h=3 and an inflow velocity of 3 KN. The drag results obtained from these meshes were then compared:

Table 1. Drag Numerical Results for Models with Different Mesh Counts.

Number of Mesh Cells (million)	1.49	2.76	5.75
Drag (N)	616.68	592.97	594.56

From Table 1, it can be seen that the drag results show an error of 3.99% between the 1.49 million and 2.76 million mesh counts, and an error of 0.27% between the 2.76 million and 5.75 million mesh counts. Once the mesh count reaches 2.76 million, further increases in mesh quantity result in minimal changes in the numerical simulation results. Considering both computational efficiency and resource usage, a mesh size of 2.76 million is ultimately chosen.

3.3. *Numerical Method Validation*

To validate the rationality of the numerical simulation method used in this study, six sets of straight-line numerical simulations with varying inflow velocities were conducted for the standard submarine model SUBOFF. The same process parameters and configuration used in this study were applied. The drag results obtained from the numerical simulations were compared with the original drag test data of the SUBOFF model[13]. The SUBOFF shape and the computational flow domain are shown in Figure 4. A comparison between the simulation data and experimental data is shown in the following Table 2.

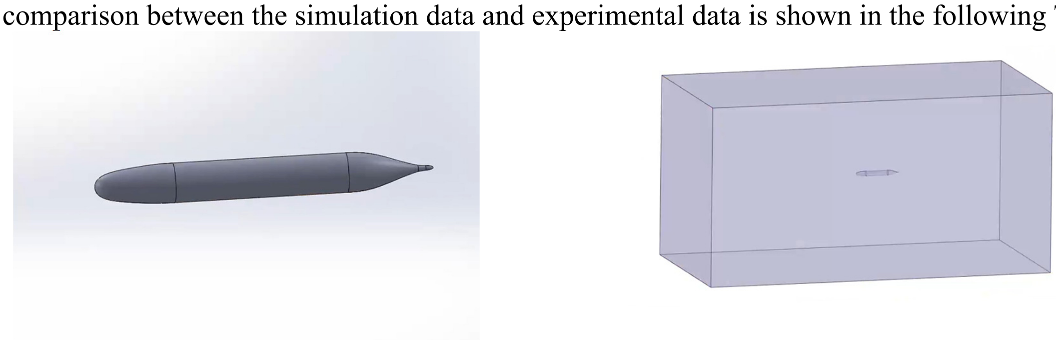

(a) (b)

Figure 4. (a) SUBOFF Model. (b) Computational Fluid Domain.

Table 2. Comparison of Experimental Data and Simulation Results

Velocity (KN)	SUBOFF Drag (N) Experimental Results	SUBOFF Drag (N) Simulation Results	Error (%)
5.92	87.4	88.6	1.37%
10	242.2	234.7	3.09%
11.84	332.9	321.4	3.45%
13.92	451.5	434.5	3.76%
16	576.9	563.2	2.37%
17.99	697.0	700.9	0.56%

From the data comparison, it can be seen that the numerical simulation results have an error of less than 5% compared to the original drag test results of the SUBOFF model, showing a good agreement and meeting the engineering requirements.

4. Computational Results

4.1. Effect of Spacing Ratio at Different Speeds

When the angle of attack is 0, the cruising speed is selected to vary from 1knto 5kn, with an interval of 1KN. The variation of the drag coefficient and lift coefficient of the AUV with the spacing ratio at different speeds is shown in Figures 5 :

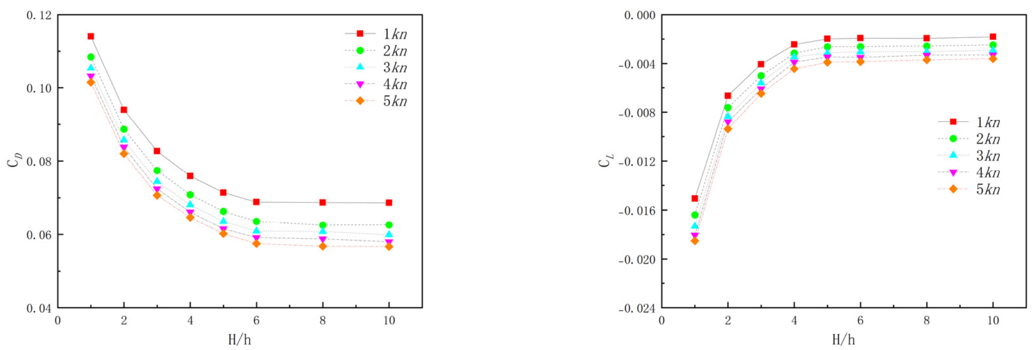

(a) (b)

Figure 5. (a) Variation of Drag Coefficient with Spacing Ratio. (b) Variation of Lift Coefficient with Spacing Ratio.

As shown in Figure 5 (a), the drag coefficient varies most significantly when the spacing ratio is between 1 and 4. The drag coefficient of the AUV decreases as the spacing ratio increases. When the spacing ratio reaches 4, the rate of change in the drag coefficient slows down, and when the spacing ratio reaches 6, the drag coefficient stabilizes and no longer fluctuates significantly. At this point, the influence of the underwater charging platform on the AUV's drag can be approximated as negligible. In the simulation, both the AUV and the underwater charging platform surfaces are treated as no-slip walls. Due to the retention effect, the flow velocity near the wall slows down. As seen in Figures 6 and 7, as the spacing ratio between the AUV and the underwater charging platform decreases, the retention effect of the fluid near the AUV's wall becomes more pronounced, leading to increased pressure at both ends of the AUV, which in turn causes an increase in drag.

For the lift coefficient of the AUV, the variation in the lift coefficient is most pronounced when the spacing ratio changes from 1 to 4, after which the change gradually slows down. As the AUV gets closer to the underwater charging platform, the hydrodynamic interference from the platform becomes stronger. The distance between the AUV's lower surface and the charging platform's upper surface decreases, and the inflow forms a continuously narrowing channel between the AUV's bottom surface and the platform's upper surface. According to the principle of mass conservation, the contraction of the flow path leads to an increase in flow velocity. At the same time, the static pressure of the fluid in the region of increased flow velocity on the AUV's bottom surface decreases, creating a pressure difference between the upper and lower surfaces of the AUV.

As shown in Figures 6 and 7, as the AUV moves closer to the underwater charging platform, the fluid velocity below the AUV increases, and the low-pressure area below the AUV becomes larger, while the pressure region above the AUV changes little. The pressure difference between the top and bottom surfaces increases, leading to a rise in lift. At the same time, from Figures 5, it can be observed that the trends of drag and lift coefficients of the AUV at different speeds are the same as the spacing ratio changes. This indicates that the interference from the underwater charging platform has a consistent effect on both the drag and lift performance of the AUV, regardless of speed.

The velocity distribution and pressure distribution contour plots for the AUV at a speed of 3 KN under different spacing ratios are shown in Figures 6 and 7:

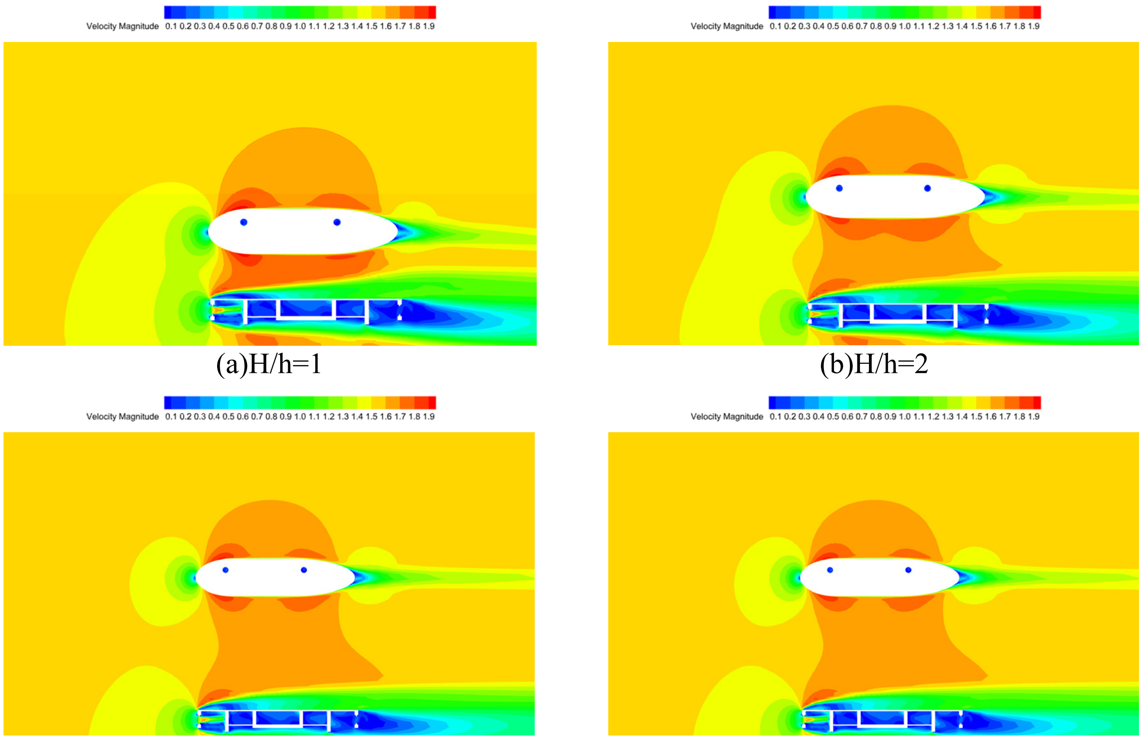

(a)H/h=1 (b)H/h=2

(c)H/h=3 (d)H/h=6

Figure 6. Velocity Contour Plot at a Speed of 3 KN for Different Spacing Ratios.

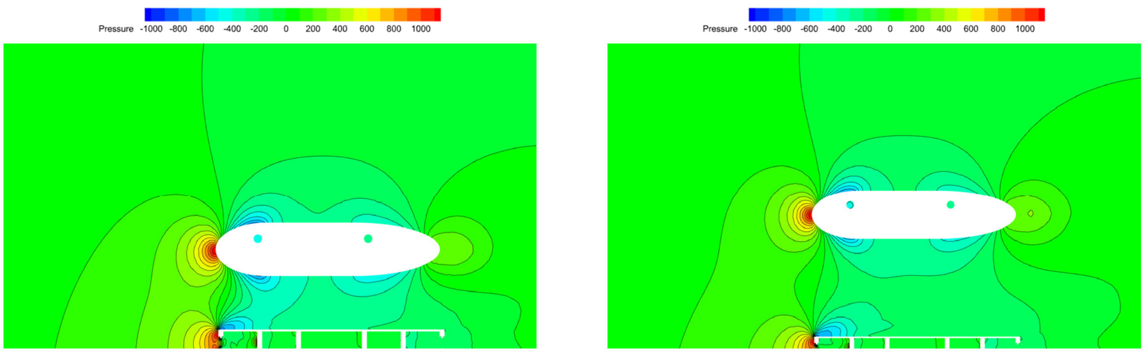

(a)H/h=1 (b)H/h=2

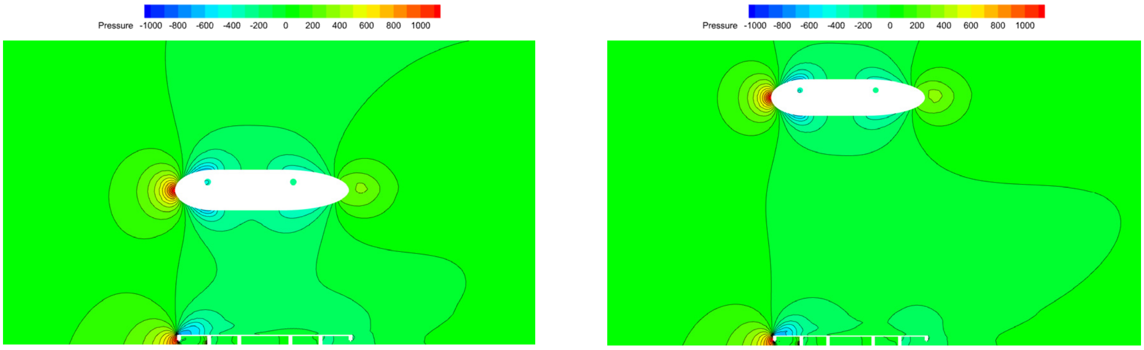

(c)H/h=3 (d)H/h=6

Figure 7. Pressure Contour Plot at a Speed of 3 KN for Different Spacing Ratios.

For the cases with spacing ratios of 1, 3, and 6, and a speed of 3 KN, the surface pressure distribution along the longitudinal cross-section of the AUV is shown in Figure 8.

"l_X" represents the distance from the AUV surface point to the bow of the AUV along the Z-axis, and PPP represents the surface pressure on the AUV. From the longitudinal cross-section pressure distribution of the AUV, it can be observed that the trend of surface pressure variation under different spacing ratios is basically the same, with no significant changes. From the zoomed-in view, it can be seen that as the spacing ratio decreases, the negative pressure on the AUV surface increases significantly, and the pressure difference between the upper and lower surfaces keeps increasing. This results in an increased suction force, which adversely affects the AUV's docking with the underwater charging platform.

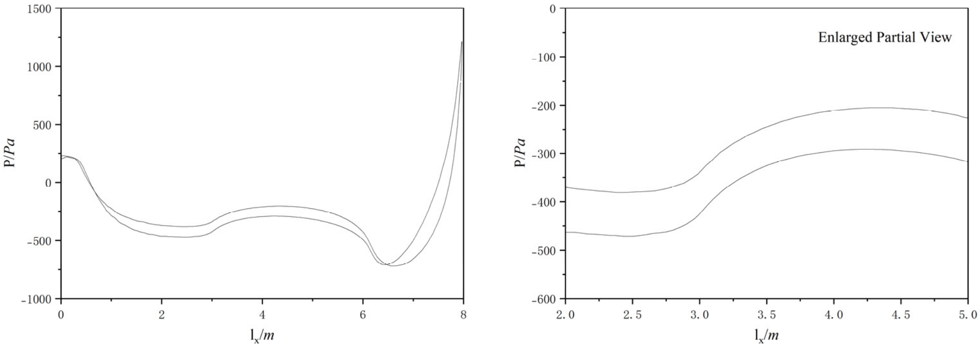

(a)H/h=1

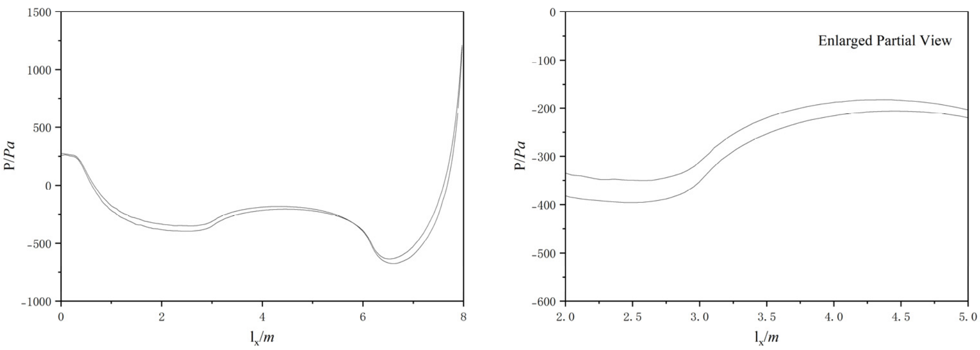

(b)H/h=3

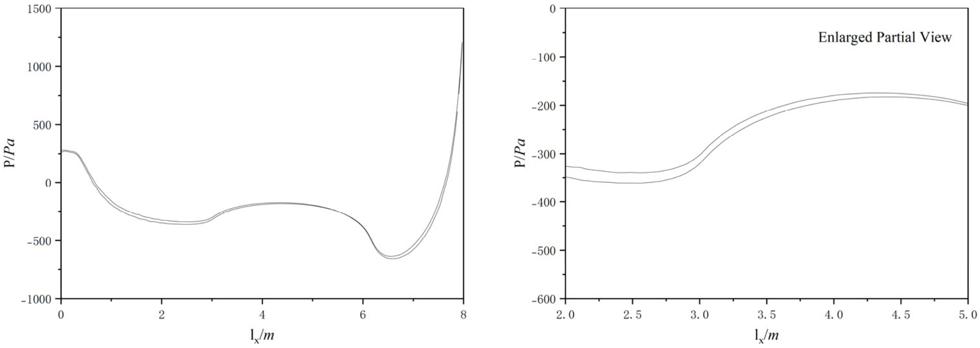

(c)H/h=6

Figure 8. Longitudinal Cross-Section Pressure Distribution of the AUV at a Speed of 3 KN for Different Spacing Ratios.

4.2. Effect of Angle of Attack at Different Speeds

The distance ratios between the AUV and the underwater charging platform were set to 1, 3, and 5, with a cruising speed of 2 kn , 3 kn and 4 kn. The drag and lift coefficients of the AUV were analyzed as functions of the attack angle, with selected attack angles of ±2°, ±3°, ±4°, ±6°, and ±9°, using the conditions at 0° as a reference. The results are shown in Figures 9.

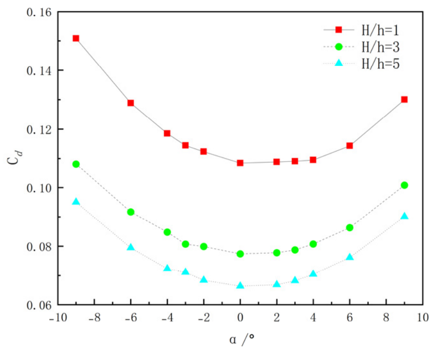

(a) 2kn

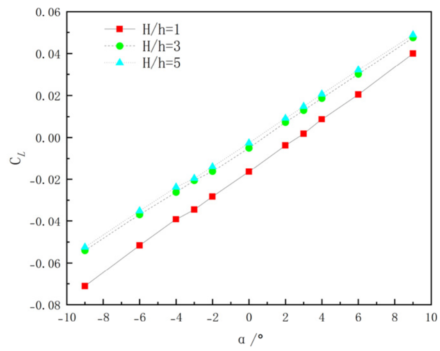

(b) 2kn

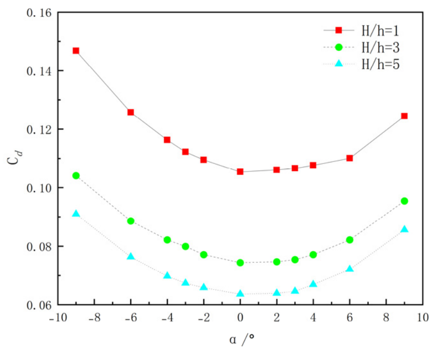

(c) 3kn

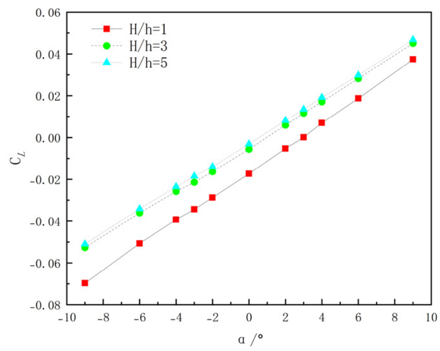

(d) 3kn

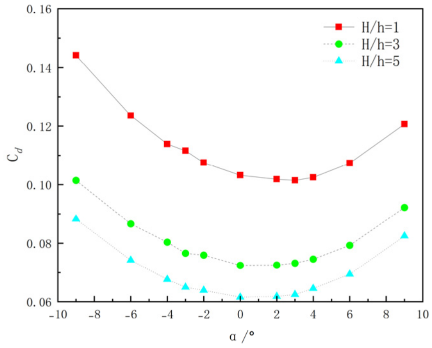

(e) 4kn

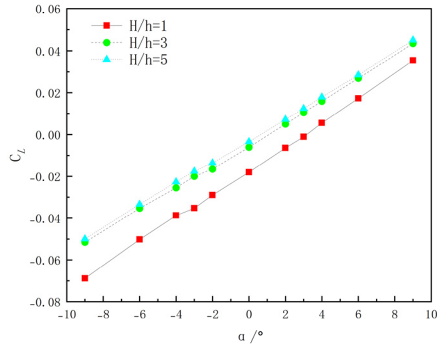

(f) 4kn

Figure 9. (a) (c) (e) The variation of the drag coefficient with the attack angle. (b) (d) (f)The variation of the lift coefficient with the attack angle.

Figure 9 (a) (c) (e) shows that the variation pattern of the AUV's drag coefficient with the angle of attack is the same at different cruising speeds. The effect of angle of attack variation on the AUV's drag performance does not change with cruising speed. The variation of the drag coefficient with the attack angle follows a similar trend across different distance ratios. The drag coefficient is minimized when the AUV has a 0° attack angle. It increases with the attack angle for both positive and negative angles. At a 0° attack angle, the AUV’s reference area is minimal, and as the attack angle increases, both the reference area and drag coefficient increase accordingly.

Figure 9 (b) (d) (f) illustrates the lift coefficient of the AUV. At negative attack angles, the lift coefficient increases with the attack angle, remaining negative, which indicates a suction force between the AUV and the underwater charging platform. At positive attack angles, the lift coefficient also increases, becoming positive and resulting in an upward lift on the AUV. Changes in cruising speed do not alter the inherent relationship between the AUV's lift coefficient and the angle of attack. The impact of angle of attack on lift performance is independent of cruising speed.From the pressure contour plots of the AUV’s mid-longitudinal section and surface pressure at different attack angles, it can be observed that, at negative attack angles, the AUV’s bow is closer to the platform wall. The fluid velocity beneath the bow is higher than that near the tail, causing a larger low-pressure zone beneath the bow and a smaller one beneath the tail. This pressure difference, with higher pressure on the upper side than on the lower side, results in a negative pressure coefficient. The surface pressure plot further shows that as the attack angle increases, the high-pressure region at the bow shifts upward, increasing the pressure differential and, consequently, the lift coefficient. The opposite occurs at positive attack angles.
Taking the condition with a cruising speed of 3 knots and a distance ratio of 3 as an example, the mid-longitudinal section and surface pressure contour plots of the AUV at attack angles of ±3°, ±6° and ±9° are shown in Figures 10 and 11.

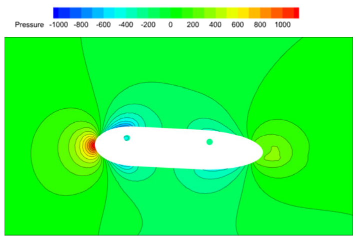

(a)α=3

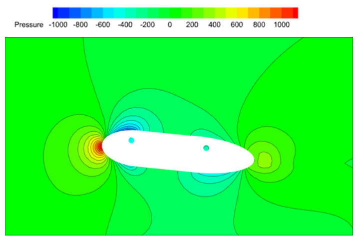

(b)α=6

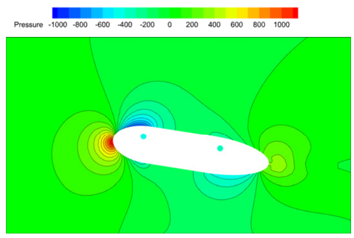

(c)α=9

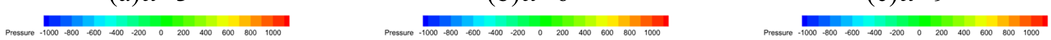

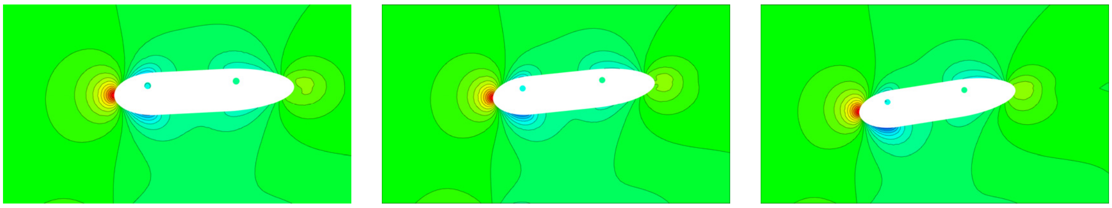

(d)α=-3 (e)α=-6 (f)α=-9

Figure 10. The pressure distribution contour plots at different attack angles.

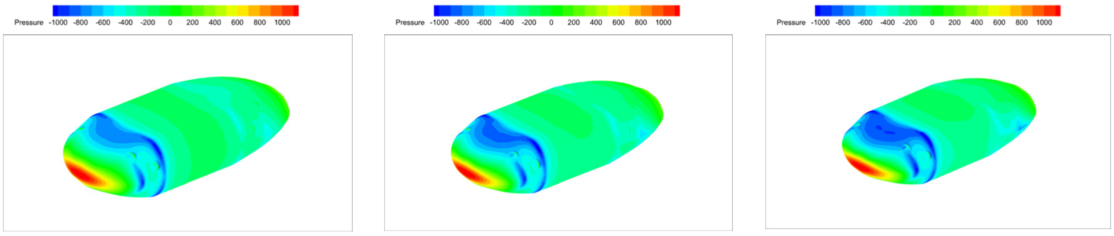

(a)α=3 (b)α=6 (c)α=9

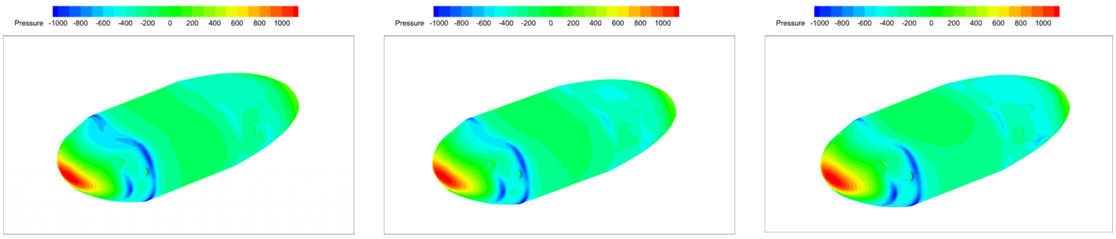

(d)α=-3 (e)α=-6 (f)α=-9

Figure 11. The surface pressure contour plots of the AUV at different attack angles.

5. Conclusion

Through hydrodynamic performance simulations of the AUV in proximity to the underwater charging platform, the following conclusions can be drawn: The variation patterns of the AUV's drag and lift coefficients with spacing ratio and angle of attack are the same at different cruising speeds. The influence of the underwater charging platform's interference and angle of attack variation on the AUV's drag and lift performance remains essentially unchanged with cruising speed;As the AUV approaches the platform, the hydrodynamic interference increases; with a decreasing distance ratio (H/h), both the drag and lift coefficients increase. When the distance ratio (H/h) exceeds 6, the platform's effect on the AUV can be considered negligible. Both the drag and lift coefficients increase as the attack angle increases. The lift coefficient is positive at positive attack angles and negative at negative attack angles. When the AUV performs a posture change near the charging platform, it should aim for positive attack angles to minimize the risk of accidental contact with the platform.

Acknowledgments

This work was financially supported by the the National Key Research and Development Program of China (Grant No.2024YFB4710803).

References

[1] Liu J, Yu F, He B, and Soares C G (2024) A review of underwater docking and charging technology for autonomous vehicles. Ocean Engineering., 297: 117154.
[2] Wang Y, Wang P and Sun P (2021) Overview of Control Technologies for Autonomous Underwater Vehicles. World Sci-Tech Research and Develop., 43: 636-648.

[3] Yin Q (2023) Research on Interference-Resilient Fault-Tolerant Control Methods for AUVs Based on Disturbance and Fault Estimation. Qingdao University.
[4] Che G and Yu Z (2020). Neural-network estimators based fault-tolerant tracking control for AUV via ADP with rudders faults and ocean current disturbance. Neurocomputing., 411: 442-454.
[5] Yazdani A M, Sammut K, Yakimenko O and Lammas A (2020) A survey of underwater docking guidance systems. Robotics and Autonomous systems., 124: 103382.
[6] Alghamdi R, Dahrouj H., Al-Naffouri T Y and Alouini M S (2023). Toward immersive underwater cloud-enabled networks: Prospects and challenges. IEEE BITS the Information Theory Magazine., 3: 54-66.
[7] Zhou J, Si Y and Lin Y (2023) A review of subsea AUV technology. Journal of Marine Science and Engineering., 45:1–12.
[8] Chen K, Du D, Xu J and Guo F (2017) Numerical Simulation of the Flow Field for SUBOFF Submarine AUV Recovery. Journal of Ship Mechanics., Z1: 68-75.
[9] Wu L, Wang S, Feng X, Li Y and Liu K (2020) Physics-Based numerical simulation of AUV autonomous docking. Journal of Beijing University of Aeronautics and Astronautics., 46: 683-690.
[10] Li Y, Li Y, Wang X, Pan Z and Xiao Z (2024) Numerical simulation of hydrodynamic performance for UUV underwater dynamic Deployment and Recovery. Ship Science and Technology., 46: 88-91.
[11] Wang M (2023) Numerical Simulation of Water Flooding in Subway Stations and Research on Disaster Prevention and Mitigation Strategies. Henan University of Technology.
[12] Du X, Wang H, Hao C and Li X (2014). Analysis of hydrodynamic characteristics of unmanned underwater vehicle moving close to the sea bottom. Defence Technology., 10:76-81.
[13] Li X, Zhang D, Zhao M, Wang X, and Shen, Y (2024) Hydrodynamic analysis and drag-reduction design of an unmanned underwater vehicle based on computational fluid dynamics. Journal of Marine Science and Engineering., 12:1388.